ORIGINAL PAPER

Steam Oxidation of Zirconium–Yttrium Alloys from 500–1100 °C

Peter Mouche[1] · Brent Heuser[2]

Abstract

The steam oxidation kinetics, oxide formation, and hydrogen uptake of nuclear-grade Zr with 0.01–12 wt% yttrium were studied. Metallography and diffraction of the as-received material showed yttrium remained trapped in solid solution in concentrations up to 2 wt%; therefore, steam oxidation focused on 0.01–1 wt% Y samples. Thermogravimetric analysis was performed in a steam–argon environment at 500 °C, 700 °C, 900 °C, and 1100 °C at atmospheric pressure. At 500 °C and 700 °C, increasing the yttrium concentration increased the total weight gain by up to 300% and caused an increase the oxidation power-law exponent. At 900 °C, increasing the yttrium concentration caused a much smaller increase in the weight gain, and resulted in a decrease in the oxidation power-law exponent. At the highest temperature, 1100 °C, increasing the yttrium concentration had a minimal effect on the kinetics. Transmission synchrotron diffraction and cross-sectional optical microscopy showed significant hydrogen uptake at 500 °C and 700 °C through the formation of δ and γ zirconium hydrides. The volume of these two hydride phases increased with increasing yttrium concentration. This hydrogen uptake appears to be linked to the increase in the steam oxidation power-law exponent observed at 500 °C and 700 °C.

Keywords Zirconium · Yttrium · Steam oxidation · Hydride

✉ Peter Mouche
mouchepa@ornl.gov; mouche1@illinois.edu

Brent Heuser
bheuser@illinois.edu

[1] Oak Ridge National Laboratory and University of Illinois Urbana/Champaign, PO Box 2008, MS6138, Oak Ridge, TN 37831-6138, USA

[2] Department of Nuclear, Plasma, and Radiological Engineering, 111B Talbot Laboratory MC 234, University of Illinois Urbana/Champaign, 104 South Wright St., Urbana, IL 61801, USA

Introduction

The zirconium-based fuel cladding used in nuclear reactors is susceptible to significant hydrogen uptake during normal operating conditions leading to the formation of zirconium hydride. The nucleation of a brittle hydride phase results in a loss of cladding mechanical properties as plate-like hydrides can provide pathways for crack propagation. This type of failure mode, referred to as delayed hydride cracking, could occur in stored spent nuclear fuel [1]. Recent research has found that incorporating yttrium into zirconium alloys promotes a favorable hydride morphology [2–5]. The yttrium provides preferential sites for hydrides to nucleate, creating a dispersed hydride structure. This microstructure reduces the number of large plate-like hydrides that promote cracking. The driving force for these changes is yttrium's stronger affinity for hydrogen than zirconium. With the usefulness of using yttrium as an alloying element demonstrated, there is a need to study how yttrium changes the other mechanisms that zirconium-based fuel cladding can experience in a nuclear reactor. Publications reporting how yttrium affects the oxidation kinetics of zirconium systems are limited, with no high-temperature steam oxidation kinetics of pure Zr–Y alloys.

The earliest work studying the oxidation of Zr–Y alloys began as response to a need for oxidation resistant alloys for use in the space industry [6]. 5–50 at.% yttrium alloys were oxidized in air at 1200 °C and 1600 °C. No weight gain information was measured; however, the oxide structure and base metal were studied using X-ray diffraction (XRD), fluorescence, and electron-microprobing. It was found that at the lower temperature of 1200 °C, the Zr and Y oxidized separately, while at the higher temperature of 1600 °C, alloy melting enabled rapid yttrium diffusion through the liquid to the surface. With an adequate flux of yttrium, a continuous yttria layer grew. The key result was that in the temperature regimes studied in this work, the diffusion of yttrium through the solid zirconium/yttrium metal was not fast enough to form a continuous yttria layer. Even 50 wt% yttrium samples resulted in mixed oxides. The fast oxidation rate most likely contributed to the lack of yttrium at the oxide/metal interface. The affinity of yttrium for oxygen was observed through the formation of yttria nodes via internal oxidation inside of the base alloy.

In 1975, Nasrallah studied the oxidation of a Zr–0.5Y alloy in air up to 545 °C [7]. This work was done in conjunction with a study on the effects of doping zirconia and yttria to examine the effects on ionic conductivity. It was found that the addition of yttrium increased the oxidation rate, as compared to pure Zr, by a factor of 6. Plotting the weight gain against the square root of time gave a linear trend, indicating that the kinetics were parabolic. An Arrhenius plot of the data showed that both pure Zr and the yttrium-alloyed samples had similar activation energies for diffusion. The author concluded that the driving force for the increase in the diffusion coefficient was an increase in the concentration of oxygen vacancies due to yttrium doping.

The oxidation of pure Zr–Y alloys was not studied since the above 1975 work; however, several ternary systems of Zr, Y, and Ni or Nb have been examined for

various uses. The Zr–Y–Ni alloy studied by Fuhrmann [8] examined a range of Ni–Zr alloys from 8–82 at.% Zr, and Ni–Zr–Y alloys from 92–19 at.% Ni with a balance of Zr and Y in a ratio of 5 to 1. These were oxidized in 800 °C, 900 °C, and 1000 °C oxygen environments. The binary Ni–Zr alloys showed very minimal change in the degree of oxidation across the composition; however, the Ni–Zr–Y alloys showed orders of magnitude thicker oxide, with substantial internal oxidation of the Zr and Y leaving metallic Ni. Only the highest Zr–Y concentration formed a thick layer of yttria, causing the oxide thickness to match that of the Ni–Zr alloy. The addition of smaller concentrations of yttrium to this alloy system was detrimental to the oxidation rate.

A more interesting publication examined yttrium ion implantation in the surface of Zircaloy-4 [9]. Doses of $1 \times 10^{16}, 5 \times 10^{16}$, and $1 \times 10^{17} \frac{\text{ions}}{\text{cm}^2}$ were implanted into polished samples to a maximum depth of 70 nm. These implanted samples were then oxidized at 500 °C in air. A weight decrease from 0.15 to 0.11 $\frac{\text{mg}}{\text{cm}^2}$ over 100 minutes was observed between the as-received sample and largest dose sample. This was associated with a transition from mainly monoclinic zirconia to the tetragonal phase. No preheat treatments occurred, and the yttrium atoms remained near the surface, with a maximum concentration of 0.2 at.% peaking at 30 nm deep. Yttrium is known to stabilize the tetragonal and cubic phases of zirconia [10]; however, only the ion implanted study managed to see a large shift in the stabilization. Both Batra [3] and Fuhrmann observed the individual formation of both yttria and zirconia.

In a similar study, a yttrium surface coating 0.1 μm thick was sputter-coated onto the surface of Zircaloy-2, and then mixed with the substrate via Xe bombardment to increase adherence [11]. This resulted in a decrease in the amount of oxygen in solid solution underneath the oxide after exposure to supercritical water at 400 °C for 168 h. No weight gain information was recorded, and cross-sectional SEM did not observe a distinct yttria layer on the surface. The authors, Sridharan and Harrington, claim that doping zirconia with yttria decreases the diffusion coefficient; however, other experimental work disputes this result [12].

In an effort to reduce continuous hydride formation in reactor cladding, Batra examined how yttrium additions to Zr–Nb alloys affected both the hydride formation and oxidation resistance [3]. Accelerated autoclave exposures at 10 MPa and 400 °C were performed for 72 h, and the oxide thicknesses were measured. It was found that adding yttrium and decreasing the Nb concentration reduced the oxide thickness by a factor of four, while the hydrogen pickup fraction increased from 0.028 to 0.247. The resulting hydride morphology changed from long interconnecting plates to discrete precipitates. The increased hydrogen uptake should be noted as it is especially relevant to this work.

Experimental Procedures

Yttrium–zirconium alloy material was obtained from ATI Specialty Alloys and Compounds. The material was delivered as cast ingots of hafnium-free zirconium with 0.01, 0.1, 0.5, 1, 2, and 12 wt% yttrium. 1-mm-thick coupons were sectioned from the bulk using electrical discharge machining, and the surface oxides from the

machining process were mechanically removed. Prior to steam exposure, samples were cut into $10 \times 10 \times 1$ mm coupons using a low speed diamond saw. The two 10×10 mm faces were manually mechanically polished to 1200 grit using SiC polishing paper. Samples were then ultrasonically cleaned in acetone and methanol. Finally, sample dimensions were measured with digital caliper, or from photos taken with a known scale using ImageJ.

A NETZSCH Jupiter 441 Simultaneous Thermal Analyzer (STA) was used for the thermogravimetric analysis [13]. Correction files, which use the exact same temperature and gas profiles, were run to account for the buoyancy effect. After sample loading, the furnace pressure was pumped down to 10^{-4} mBar before back-filling with ultra high purity (UHP) argon. Throughout the duration of the heating, a positive pressure of argon was maintained, this inert atmosphere allowed for samples to reach the testing temperature with limited oxidation. An argon purge along with an argon carrier gas was used to transport the steam, produced at a rate of $2\frac{g}{hr}$, through heated lines into the furnace before venting from an outlet. Additionally, a constant 30 ml/min of argon flowed up along the sample carrier to protect the balance system. Fluctuations caused by the flowing steam and argon limited the resolution of the top loading internal balance to 50 μg. Samples were exposed to 500 °C, 700 °C, 900 °C, and 1100 °C steam for various time periods. To provide comparison oxidation kinetics, Zr from Alpha Aesar and Zircaloy-2 from ATI were also exposed to 700 °C steam.

Synchrotron diffraction was conducted in transmission geometry at the 11-ID-C beam line at the Advanced Photon Source located at Argonne National Laboratory. Diffraction data were collected in transmission geometry using a single CCD detector to capture the entire Debye–Scherrer cone starting at a minimum d-spacing of 1.365Å. Samples were mounted on a plastic grid with control motors to move the grid in the x–y plane, while keeping the z-alignment (incident beam direction) stationary. A 0.25 mm × 0.25 mm incident beam of wavelength 0.118 Å, was used. Data collection consisted of 1800 0.1 second exposures summed for each sample. Diffraction was also collected from a CeO_2 standard powder sample to calibrate both the instrument resolution as well as detector configuration.

Both electron and optical microscopy were performed on the samples to characterize topological/chemical information. A Hitachi S4700 high-resolution scanning electron microscope (SEM) was used to image samples pre- and post-exposure. Secondary electron imaging was used, with both analysis mode, and ultra high-resolution mode. Chemical information was collected using the linked Oxford instrument ISIS EDS X-ray Microanalysis System. The EDS data was used to track yttrium precipitation in the as-received samples, and to examine the oxide–metal interface post-steam exposure. Samples were mechanically polished to 1um for pre-exposure SEM, and vibration-polished to 0.05um for post-exposure SEM. The S4700 SEM is located in the Frederick Seitz Materials Research Laboratory at UIUC.

Two different Zeiss Axiovert with bright field/dark field/differential interference contrast (DIC) imaging modes were used for the post-exposure optical microscopy. Digital cameras were used for image acquisition at 20, 50, and 100×. As-received sample microscopy was conducted on an Axiovert located in the Frederick Seitz Materials Research Laboratory at UIUC. The as-received samples were polished to

1um and then etched with a 1 part hydrofluoric acid, 10 part nitric acid, 10 part sulfuric acid, 10 part water solution to reveal grain structure and yttrium precipitates.

Post 500 °C steam exposure cross-sectional microscopy samples were fabricated to reveal the oxide/metal interface using the following method. Oxidized samples were cut in half using a low speed diamond saw. After being mounted in epoxy, the samples were mechanically polished with a 1 μm diamond solution final step. Lastly, samples were vibration-polished for up to 8 h using a 0.05 μm colloidal silica suspension. The cross sections were chemically etched to reveal hydride structures using a 1 part hydrofluoric acid, 10 part nitric acid, 10 part sulfuric acid, 10 part water solution. Samples were etched by soaking a Q-tip cotton swab in the solution, and then rubbing the sample for 5 s. The samples were then immersed in tap water and stirred. The 0.01 wt% Y sample was etched for an additional 10 s.

Results and Discussion

As-Received Characterization

The H_2SO_4 in the etching solution preferentially corroded Y, resulting in better contrast in the higher weight fraction Y samples, shown in Fig. 1a. The etched patterns indicated that yttrium precipitated at both grain boundaries and at dispersed secondary phases throughout the grain. The dispersion and patterning of the yttrium precipitates indicates limited yttrium diffusion during cooling as seen by the occurrence of the ordered precipitation structures. SEM/EDS analysis of un-etched material confirmed that Y preferentially corroded. As depicted in Fig. 1b, c, yttrium
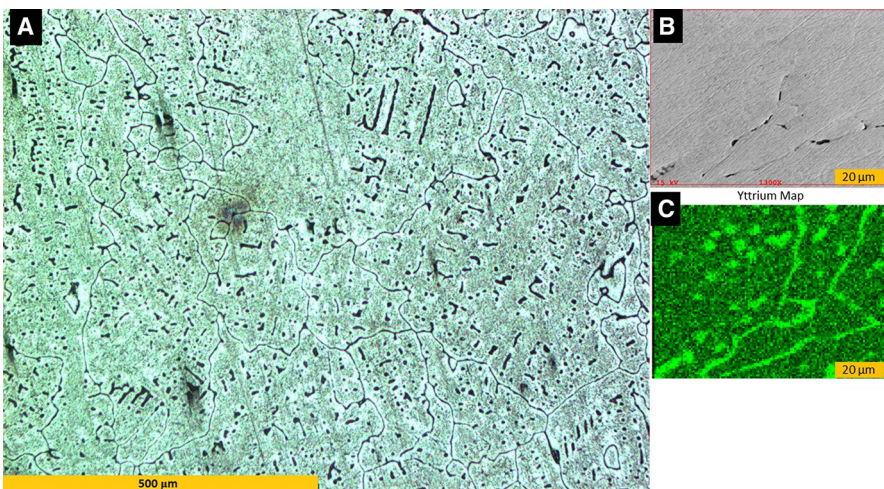

Fig. 1 **a** Optical microscopy showing grain structure of as-received 12 wt% Y. Etching preferentially removed Y, revealing precipitation at the grain boundaries and semi-organized spherical and line precipitates inside of the grains. SEM original (**b**) and EDS mapping of Yttrium concentration (**c**) before chemical etching showing grain boundary and intragranular precipitation

concentration was enriched at grains and in dispersed precipitates in a manner similar to that in the etched regions. Additionally, no yttrium enrichment was observed post-etching. The 2 wt% Y sample showed only a slight attack at grain boundaries, with some nodules in the grain boundaries. Samples containing lower Y wt% did not experience significant grain boundary attack. From the 12 and 2 wt% Y samples, a typical cast microstructure was observed: equiaxed grains in the center, larger columnar grains closer to the edge, and small grains near where the metal touched the mold. Analyzing the grain size of the sample bulk, gave an area weighted grain size of 450 µm. This large grain size was reflected by the extreme anisotropy in the azimuthal intensity of the synchrotron data. Examples of as-received diffraction patterns of the 0.01wt% and 12wt% Y are shown in Fig. 2.

From the diffraction pattern of the as-received samples, yttrium diffraction peaks were only observed in the 12 wt% Y sample. This observation of peaks only in the 12 wt% Y sample agrees with those of the metallography results. It can also be concluded that a majority of the grain boundary etching in the 2 wt% Y sample comes from yttrium enrichment and not from yttrium precipitation at the grain boundaries. The amount of yttrium in solid solution was determined by calculating a lattice parameter from d-spacing as function of yttrium concentration. After azimuthal integration, d-spacing for the (100), (110), and (200) Zr reflections was extracted from pseudo-Voigt fits of the peaks. The zirconium a lattice parameter was calculated using Eq. 1.

$$\frac{1}{d^2} = \frac{4}{3}\frac{h^2 + hj + k^2}{a^2} + \frac{l^2}{c} \tag{1}$$

Figure 3 shows that the average of the three calculated a lattice parameter values followed Vegard's law and linearly increased with yttrium concentration to 2 wt% Y.
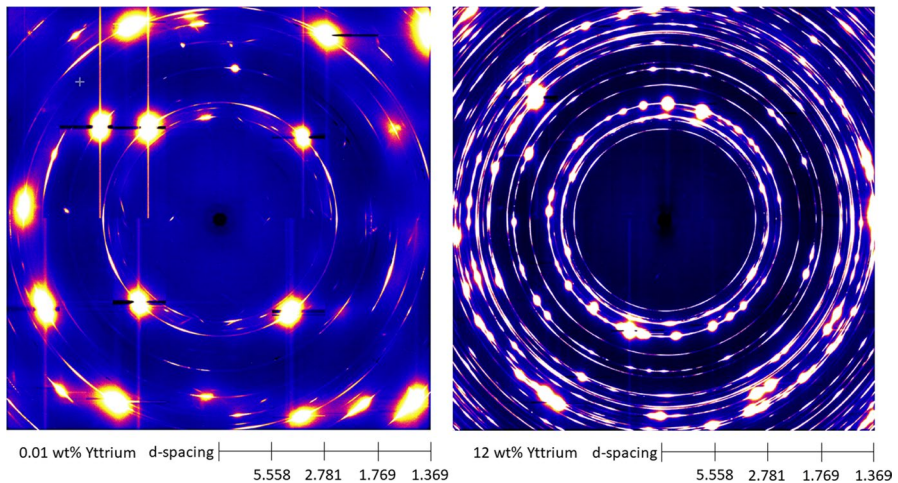

0.01 wt% Yttrium d-spacing ├──┼──┼──┼──┤ 5.558 2.781 1.769 1.369

12 wt% Yttrium d-spacing ├──┼──┼──┼──┤ 5.558 2.781 1.769 1.369

Fig. 2 Raw panel detector data from as-received 0.01 wt% and 12 wt% Y. Effect of large grain size, especially in the 0.01 wt% Y, is shown by strong individual peaks instead of diffraction rings
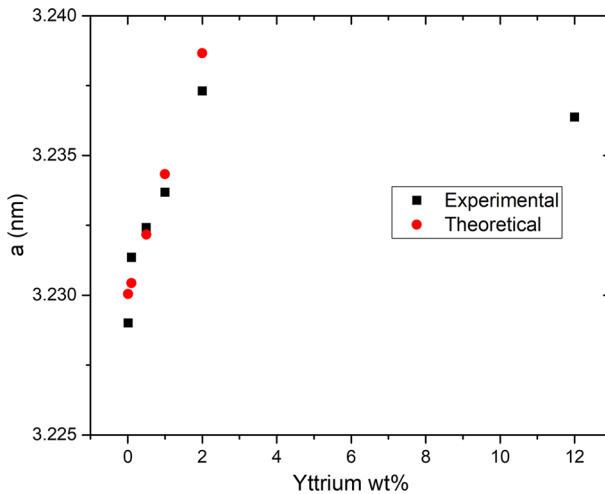
Fig. 3 Average experimental a lattice parameter for Zr in the as-received alloy as a function of the yttrium wt% Y calculated from synchrotron diffraction compared to the theoretical value

The experimental a lattice parameter values agree reasonably well with theoretical values of a two element mixed phase calculated using Eq. 2, where x is the fraction of element B, a_A is the lattice parameter of phase A, and a_B is the lattice parameter of phase B.

$$a_{A_{(1-x)}B_x} = (1 - x)a_A + xa_B \tag{2}$$

At 12 wt% Y, when yttrium precipitated out of the matrix, the lattice parameter decreased slightly. This indicates that the yttrium was in supersaturated solution. Nucleation sites allowed some of the excess yttrium to come out of solution. From the zirconium–yttrium phase diagram, less that 0.1 wt% Y should be in solid solution in zirconium at equilibrium. Therefore, the yttrium in most of the samples was in a supersaturated solid solution within the Zr matrix. This agrees with work by Peng, who observed up to 4 wt% Y remaining in solid solution in cast Zr–Y alloys [14].

Oxidation Kinetics

The oxidation kinetics studied in the STA focused on the 0.01–1 wt% Y concentration samples, where phase separation did not occur. Figure 4 shows the weight gain versus time data from the steam oxidation. The addition of yttrium systematically increased the oxidation driven weight gain at lower temperatures. At 500 °C there was a clear separation in the weight gain curves for all of the compositions due to the strong affect of the yttrium. The addition of 0.1 wt% Y increased the weight gain after 1200 minutes by ~40%, and the 1 wt% Y sample had a 300% increase in weight gain. At 700 °C both the Zr–Y along with Zircaloy-2 and "pure" Alfa Aesar zirconium as the comparison material is shown. The Alfa Aesar zirconium is listed as "pure" due to the fact that the hafnium content was not given by the
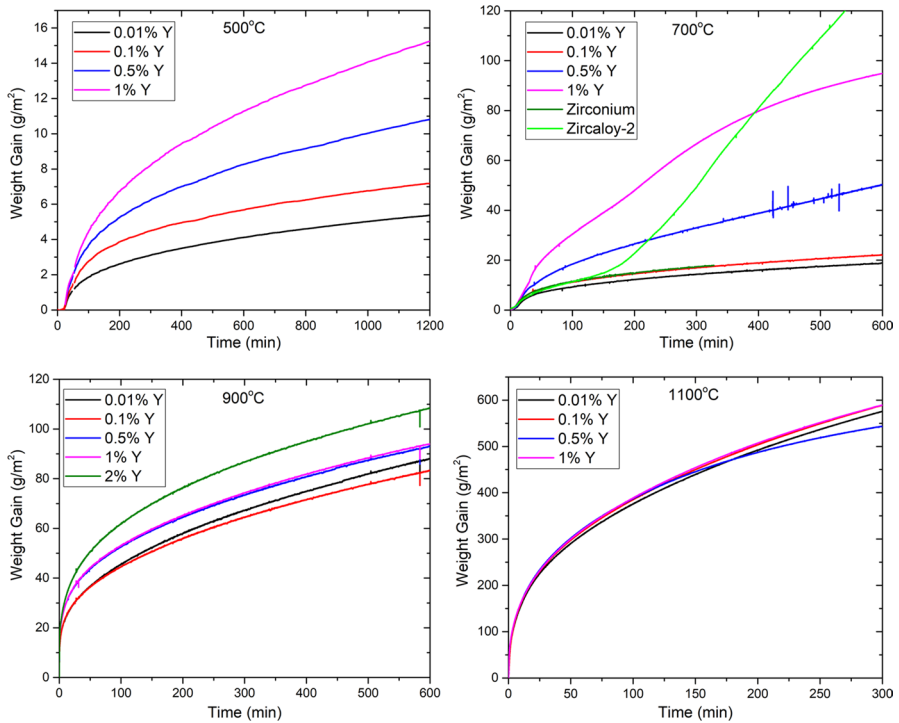
Fig. 4 Thermogravimetric data of steam oxidation kinetics at 500 °C, 700 °C, 900 °C, and 1100 °C

manufacturer. The graph of the weight gain versus time shows that the addition of yttrium still systematically increased the oxidation kinetics, but the clear separation between the 0.01 and 0.1 wt% sample is much smaller. The 0.01–0.5 wt% Y samples followed quasi-cubic oxidation throughout the duration of the experiment. Cyclic oxidation kinetics were observed in the weight gain data when the yttrium concentration reached 1 and 2 wt% Y. Each experienced two cycles, but surprisingly, the 1 wt% Y sample experienced oxide failure before the 2 wt% Y sample. No transition to pure breakaway oxidation was observed, but the oxidation kinetics for these two concentrations were multiple times larger at 600 minutes than the kinetics for the lower wt% Y samples.

As a comparison, the Zircaloy-2 sample does exhibit a standard quasi-cubic to breakaway behavior. The initial behavior followed the 0.1 wt% Y and "pure" Zr weight gain. The transition to linear breakaway weight gain at 200 minutes resulted in a greater overall weight gain than the 1 and 2 wt% Y samples past 600 minutes. This clearly demonstrates why the transition to linear oxidation kinetics should be avoided. From previous studies, impurities strongly control the time to breakaway oxidation [15]. Therefore, the oxide cracking and failure in both the Zircaloy-2 and higher Y wt% samples is expected. The "pure" Zr shows weight gain that is the same as the 0.1 wt% Y kinetics. Binary oxidation kinetics reported by Porte [16] show that the addition of hafnium slightly increases the power-law exponential which

would account for the increase in the oxidation. Therefore, Hf contamination of the "pure" Zr, since it is not nuclear grade Hf-free Zr, is the most likely reason for the increase in the oxidation rate. This also implies that the 0.01 wt% Y sample should exhibit kinetics that are very close to pure Zr oxidation.

At 900 °C the weight gain curves began to converge across the compositions. At this temperature, increasing the yttrium concentration from 0.01 to 2 wt% only increases the weight gain after 600 minutes by ∼ 12%. At the highest temperature, 1100 °C, minimal differences were observed in the oxidation kinetics.

Kinetics Fitting

To understand the differences in the weight gain curves, data were fit to the basic power-law oxidation equation

$$x = kt^n \tag{3}$$

where x is the oxide thickness and t is the time. The Arrhenius temperature effects and diffusion constant are combined in k. n is an indication of how self-limiting the oxide is. $n = 1$ is a non-protective oxide, while $n = 0.5$ is a standard diffusion limited oxidation value. For pure Zr, $n = 0.33$ is commonly observed [16]. The data were fit on a log/log scale to obtain the exponent n and k. This was done to ensure that the regions fit followed a steady-state power-law rate. It was observed that the first few minutes of the oxidation followed linear or faster than linear oxidation kinetics. It was determined that this was caused by a reactant limited oxidation process. After steam was released into the system, it took a set period of time at each temperature to saturate the furnace causing the partial pressure of the steam, and therefore the weight gain, to increase with time. Therefore, only the data from the latter part of the oxidation time were fit. Table 1 lists fitting results of the data to Eq. 3.

The k values show the expected increase with temperature, as the diffusivity follows an Arrhenius behavior. Focusing on the changes of k with yttrium concentration, the 0.01% Y samples have a consistently lower k value than the other samples, but no clear trend is observed with increasing Y concentration between all of the samples, aside from an overall increase in the value when yttrium was present. An increase in the k value was expected based on the results from Nasrallah's work [7]; however, a majority of the increase in the weight gain appears to come from changes in the power-law exponent. At all four temperatures, the 0.01% Y samples

Table 1 Steam exposure kinetics fitting results

Temp.	k ($\frac{g}{m^2}/t^n$)				n			
	0.01% Y	0.1% Y	0.5% Y	1% Y	0.01% Y	0.1% Y	0.5% Y	1% Y
1100 °C	64.67	65.92	73.96	67.91	0.38	0.38	0.36	0.38
900 °C	8.11	8.58	11.66	11.67	0.37	0.35	0.32	0.33
700 °C	1.53	1.93	1.41	1.87	0.39	0.38	0.56	0.61
500 °C	0.35	0.71	0.72	0.70	0.39	0.34	0.38	0.44

had very similar n values. At 500 °C and 700 °C, initially adding yttrium to 0.1 wt% decreased n; however, greater Y concentrations were associated with increasing *n*. At 900 °C a steady decrease in n was observed with increasing Y, and at 1100 °C n was fairly constant. The changes in n can be divided in to three regimes, which will be discussed later.

Post-Exposure Phase Characterization

Synchrotron diffraction performed at the Advanced Photon Source measured both the thermally grown oxides, and zirconium phase evolution of the post-STA-steam exposed samples. Figure 5 shows example diffraction spectra from the 0.01–2 wt% yttrium samples after 10 h of steam oxidation at 700 °C. Only a select region of the spectra is shown to prevent peak overcrowding; all phases present in the samples exhibit peaks in this region. Both the monoclinic and tetragonal phases of zirconia were present in the synchrotron diffraction data of all oxidized samples. Across the various samples, the other diffraction peaks were observed due to an oxygen ordering in the hexagonal α - zirconium phase at a non-stoichiometric Zr_3O composition, yttria, γ and δ zirconium hydrides, and a yttrium hydride. Table 2 summarizes which phases were observed via synchrotron diffraction in steam.

The fraction of the ordered Zr_3O sub-oxide to Zr increased with increasing temperature, with no Zr_3O present at 500 °C and almost all of the Zr transformed into Zr_3O at 1100 °C. The Zr_3O structure has been observed previously by both synchrotron diffraction, transmission electron microscopy (TEM), neutron diffraction, and computational work [17–20]. The TEM work identified the sub-oxide as forming at the oxide/metal interface when samples were oxidized at 500 °C. From diffraction research by Holmberg and Yamaguchi [21, 22], the Zr_3O sub-oxide becomes distinguishable by diffraction when oxygen atoms, which are usually randomly distributed
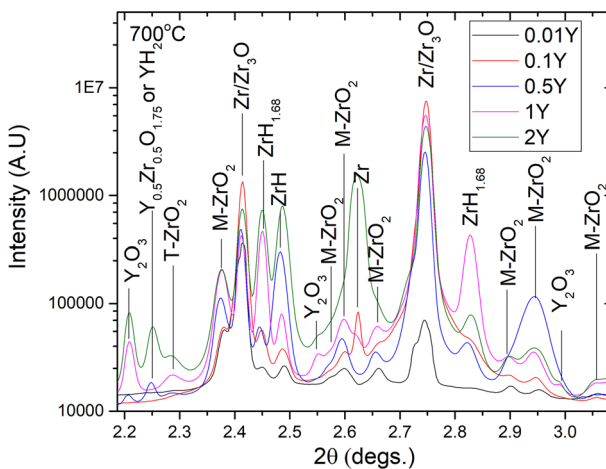

Fig. 5 Representative synchrotron diffraction data from 10 h 700 °C steam exposed samples. Over-saturated Zr diffraction peaks were masked

Table 2 Non-zirconia phases observed in synchrotron diffraction after steam oxidation

Yttrium wt% Y	500 °C 20 h	700 °C 0.5 h	700 °C 10 h	900 °C 10 h	1100 °C 5 h
2%		Zr Hydrides, Zr_3O, Yttria	Zr/Y Hydrides, Zr_3O, Yttria		Zr_3O, Yttria
1%	Zr Hydrides	Zr Hydrides, Zr_3O, Yttria	Zr Hydrides, Zr_3O, Yttria	Zr Hydrides, Zr_3O, Yttria	Zr_3O, Yttria Zr Hydride
0.5%	Zr Hydrides	Zr Hydrides, Zr_3O	Zr/Y Hydrides, Zr_3O, Yttria	Zr Hydrides, Zr_3O, Yttria	Zr_3O, Yttria
0.1%	Zr Hydrides	Zr Hydrides, Zr_3O	Zr Hydrides, Zr_3O	Zr Hydrides, Zr_3O, Yttria	Zr_3O, Yttria
0.01%	Zr Hydrides	Zr Hydrides, Zr_3O	Zr Hydrides, Zr_3O	Zr Hydrides, Zr_3O	Zr_3O

in the octahedral interstitial sites at low concentrations, form a super lattice. This occurs at a composition of $ZrO_{0.35}$ and slightly shifts the diffraction to lower angles. The shift is clearly seen in Fig. 5 by the two overlapping peaks at 2.75° in the 0.01 wt% Y sample, where masking of a majority of the Zr intensity due to detector over-saturation revealed the smaller Zr_3O. At the higher yttrium concentrations, the Zr_3O peak is present as a smaller shoulder on the Zr peak. Additional O added to the matrix above the 0.35 O concentration continues to be randomly distributed, but the O super lattice remains. This mechanism behind the ordering and associated change in diffraction spectra for Zr_3O explains the synchrotron results observed in this study. At higher temperatures, greater amounts of oxygen can exist in solid solution in the metal, and the O can rapidly diffuse through the bulk at higher temperatures. With greater consumption of the metallic Zr, the amount of oxygen in solid solution increases and becomes more evenly distributed, resulting in a greater fraction of Zr_3O upon cooling. At 500 °C, the concentration of O in solid solution was not high enough to form the super lattice.

The formation of yttria appeared to be linked to the degree of oxidation, with less yttria observed at lower temperatures and shorter oxidation times. No yttria diffraction peaks were found in 20 h 500 °C steam exposed samples. After 30 minutes at 700 °C, yttria only formed at 1 and greater wt% Y, while after 10 h it formed at 0.5 and above wt% Y. At 900 °C and 1100 °C, yttria formed at 0.1 and above wt% Y. No yttria was observed in the synchrotron diffraction pattern of the 0.01 wt% Y sample.

Hydrides formed in all samples below 1100 °C. The zirconium hydrides formed in both the δ ($ZrH_{1.68}$) and γ (ZrH) phases. The γ zirconium hydride phase is known to form under cooling rates greater than 10 °C per minute [23, 24]. Very weak hydride diffraction was observed in the 1 wt% 1100 °C sample; however, the intensity was negligible compared to the lower temperature samples. Further analysis of the hydride phase is presented in the next section.

At 700 °C, a particular phase was present that was only observed at this temperature, and only in the 0.5 and 2 wt% Y samples. This phase is either a mixed zirconium/yttrium oxide of composition $Y_{0.5}Zr_{0.5}O_{1.75}$, or a yttrium hydride. Both of these phases belong to the cubic Fm-3m space group and have almost identical a lattice parameters of 5.205Å. Therefore, all reflections occur at the same d-spacing and are differentiated by peak intensity. Since only the strongest (1 1 1) peak was isolated, it was not possible to determine which phase had formed from the diffraction pattern. However, given the strong affinity of yttrium for hydrogen, the yttrium hydride phase is the most probable structure. The $Y_{0.5}Zr_{0.5}O_{1.75}$ phase was reported from a study examining sintered oxide powders [25]. In this study, stoichiometric ZrO_2 and Y_2O_3 were compressed into pellets at 3 ton/cm^2, and then air-fired at temperatures of approximately 1475 °C. Given the conditions needed to form this compound, it is plausible to assume that the diffraction peak observed in this study was from yttrium hydride

Effect of Yttrium on Hydride Intensity

The strong, near-single-crystal Zr diffraction peaks from the large Zr grains made whole pattern fitting difficult. Over-saturation of several strong Zr peaks

required masking of the data in many diffraction patterns and the bulk Zr induced strong texturing in the oxides and hydrides. Therefore, to determine the amount of hydrogen uptake as a function of Y concentration, the peak areas of select monoclinic zirconia and zirconium hydride reflections were fit to a pseudo-Voigt function.

Zirconia was used to normalize these hydride peak intensities since the amount of hydrogen produced is controlled by the amount of oxidation. The degree of oxidation between the 0.01 and 1 wt%Y samples differed by up to 3× at 500 °C necessitating this normalization. For zirconia, the (−1 1 1) peak was selected, as it was both isolated, and had a medium strength intensity with no over-saturation. The (1 1 1) and (2 2 0) δ hydride peaks, and the (1 1 1) γ hydride peak were selected for comparison. When calculating hydrogen uptake, the δ and γ hydride intensities were summed to give the total hydride amount. Table 3 lists the comparison of hydride-to-oxide intensity at 500, 700, and 900 °C, as well as a comparison between the δ and γ intensities at 500 °C.

From these data, three features can be seen: (1) The zirconium hydride to monoclinic zirconium oxide ratio increased with increasing yttrium concentration. (2) The magnitude of the increase decreased with increasing temperature. (3) The intensities of the (1 1 1) and (2 2 0) δ hydride phase increase with respect to the γ phase as a function of yttrium wt% at 500 °C. The increasing hydrogen uptake with increasing yttrium concentration mirrors Batra's observations from autoclave experiments [3]. The decrease in the fraction of γ zirconium hydride agrees with results found by Lanzani [26]: increasing impurity concentrations in Zr decreases the stability of γ hydride, resulting in more δ hydride.

To support the results of the hydride peak intensity fitting, the post-steam exposure hydride structure was investigated with optical microscopy. The 500 °C samples were used due to the large difference in hydride concentration from 0.01 to 1 wt% Y. After cross-sectioning and vibration polishing, hydride precipitates were observed via two different methods: differential interference contrast (DIC) and acid etching. Using the differential interference contrast (DIC) imaging mode, surface features were revealed that were not seen in either the bright field or dark field. Figure 6 shows DIC optical microscopy of the bulk zirconium of

Table 3 Normalized hydride peak area comparisons

	Yttrium wt%			
	0.01	0.1	0.5	1
500 °C				
Hydride-to-oxide intensity	7.1	16.5	21.5	87.8
γ to (1 1 1) δ	3.6	1.4	0.9	0.2
γ to (2 2 0) δ	5.9	5.1	1.0	0.04
700 °C				
Hydride-to-oxide intensity	0.1	2.6	15.9	11.0
900 °C				
Hydride-to-oxide intensity	0.1	1.6	3.9	8.5

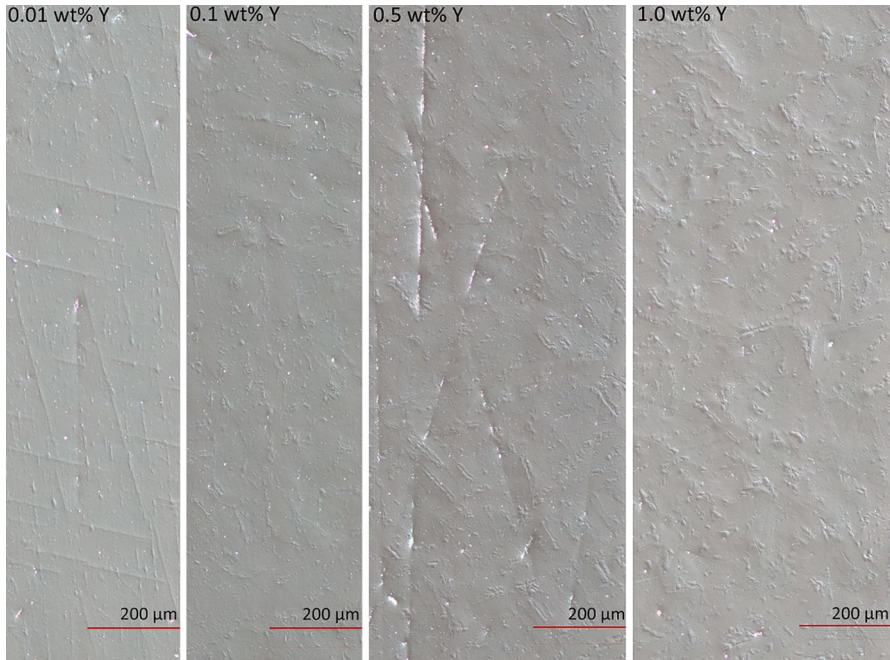**Fig. 6** Cross-sectional optical microscopy of 500 °C samples post-steam exposure. Multiple images were taken in DIC mode at 50× and stitched together to show small variations in sample roughness. Contrast is from hydrides

the 0.01–1 wt% Y samples after 500 °C 20-h steam exposure. Significant surface topology can be seen that both increase in complexity and changes with yttrium concentration.

The many ways in which these features evolved with increasing yttrium concentration indicate that they are hydrides. The density increases with increasing yttrium concentration, and the evolution of the structure follows the same changes in hydride morphology observed by Batra [3] when yttrium was added to zirconium: plate-like to dispersed morphology. To confirm that the structures were zirconium hydrides, the samples were chemically etched for 5 s with an acid solution that preferentially attacked zirconium hydride phases. By overlaying optical microscopy images, it was found that the regions of the samples most strongly etched corresponded precisely with the features observed in DIC. The etching also revealed smaller hydride structures that were not visible with DIC, as seen in Fig. 7.

Combining the results from both DIC and etching, gave a well-rounded picture of the zirconium hydride evolution. At 0.01 wt% Y, hydrides precipitated on zirconium habit planes, as seen by the long, parallel hydrides in the DIC imaging. Hydrides have several preferred planes in which to grow [27]. Phase field simulations have found that the δ Zr hydride habit plane is the (0001), perpendicular to the c axis [28]. Given the large grain size of the system, hydride nucleation inside of the grain would most likely occur along these planes. Minimal etching occurred after 5 s, with some of the long parallel hydrides revealed, and additional etching resulted in
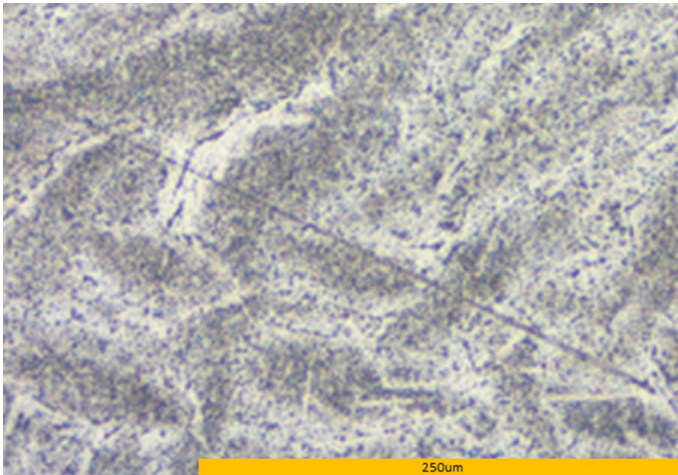
Fig. 7 Cross-sectional optical microscopy of 500 °C samples post-steam exposure. Contrast is from preferential hydride attack after 5 s of etching. Denuded zones can be seen around larger hydrides

corrosion of the bulk Zr. This was due to the overall low hydride concentration in this sample. With the 0.1 wt% Y sample, the hydride concentration was sufficient that 5 s of etching revealed a clear microstructure with hydrides preferentially precipitating at grain boundaries. Where grain boundaries intersected, larger hydrides formed that were responsible for the contrast in the DIC imaging mode.

At 0.5 and 1 wt% Y, hydrides precipitated both intragranularly and at grain boundaries. A majority of the intragranular hydrides were not observed in the DIC mode, but were revealed by etching as small dispersed hydrides in the center of the grains. The short distances between the small intragranular hydrides resulted in what appeared to be a uniform etch, rather than distinct points. In these samples, the large grain boundary and intragranular hydrides locally reduced the hydrogen concentration, creating denuded zones free of the small, dispersed intragranular hydrides, as shown in Fig. 7.

The addition of yttrium has a clear effect on the hydride structure from the 0.01 wt% Y to 1 wt% Y. The addition of yttrium reduced the precipitation along preferential planes, and caused nucleation at the grain boundaries. Additionally, the total hydride fraction increased, as seen by both the degree of preferentially attacked regions after 5 s of etching, and the number of hydride structures in the DIC imaging mode. Furthermore, from the etching, significant dispersed hydride nucleation occurs inside of the grains of both the 0.5 wt% Y (not shown) and 1 wt% Y samples. A quantitative analysis of the hydride fraction from the etching is difficult to perform for several reasons. At the 0.01 wt% Y, the hydride concentration is small such that the base Zr is significantly corroded in the time necessary to fully etch and reveal the hydrides. At 1 wt% Y, the dispersed small intragranular hydrides cannot be properly quantified. Lastly, the features shown in the DIC imaging mode only represent the largest hydrides. However, qualitatively the interpretations of the hydride microscopy agree with those of the synchrotron diffraction:

increasing yttrium concentration increases the hydrogen uptake during steam oxidation. It should be noted that the synchrotron diffraction cannot probe hydrogen that is trapped in solid solution during rapid cooling. The magnitude of this effect should be minimized by the fact that once hydrogen precipitation occurs in a supersaturated zirconium lattice, hydride grown will continue until the TSS_D is reached [29]. Therefore, unless the TSS_D of the system is dramatically changed by the yttrium, the base concentration of hydrogen in the samples that cannot be measured by diffraction will remain constant at the TSS_D since precipitation occurred in all of the low temperature samples.

Hydride-Kinetics Relationship

The steam oxidation kinetics as a function of yttrium from Fig. 1 fall into three different regimes: (1) increasing n, (2) decreasing n, and (3) constant n. At 500 °C and 700 °C, where the hydrogen uptake is large, the power-law exponent, n, increases with yttrium concentration. It is important to note that n initially decreases from 0.01 to 0.1 wt%, but increases from then on. At 900 °C, n decreases with increasing yttrium concentration. At the highest temperature, 1100 °C, n remains relatively constant, decreasing slightly with increasing yttrium concentration. This indicates that there are two different competing mechanisms. Mechanism 1 decreases n with increasing yttrium concentration and is active at all temperatures, but is not as strong at high temperatures. This mechanism is most likely yttrium doping of the oxide affecting the oxygen diffusion. Air oxidation studies of different binary alloys have observed both increases and decreases in n with increasing alloying element concentration [16]. Mechanism 2 strongly increases n with increasing yttrium concentration, but rapidly becomes weak at high temperatures. At 500 °C and 700 °C when both mechanisms are active; mechanism 1 initially decreases n at 0.1 wt%, but then mechanism 2 dominates at the higher yttrium concentration. At 900 °C and 1100 °C, mechanism 2 is not strong enough to increase n.

The hydrogen uptake appears to be linked to mechanism 2. Both increase with Y concentration, and significantly decrease at elevated temperatures. At 500 °C and 700 °C where hydrogen uptake was the greatest, increasing n is observed. Whether or not the hydrogen uptake is driving mechanism 2, or a side effect is not clear yet. Several studies have found that hydrogen uptake increases with increasing oxide resistivity [30]. The electron transport is limited by the resistivity of the oxide, creating an electric potential to facilitate the electron movement. This potential also promotes the diffusion of charged hydrogen ions into the oxide. It has been observed that this results in hydrogen uptake that increases with a *decreasing n* [31]. The increase in both hydrogen uptake and n at 500 °C and 700 °C in this work conflicts with this trend. The strong affinity of yttrium for hydrogen may be the key factor. Increasing the yttrium concentration could also drive a flux of H^+ atoms through the oxide as yttrium acts as a getter. This would cause a net current in the oxide that would need to be compensated. Further research focusing on the exact relationship between the lower temperature oxidation kinetics and hydrogen uptake has been conducted and will be presented along with a computational model to explain the

mechanisms in a following publication. This research along with additional information can also be found in the PhD dissertation that this publication is based on [32].

Comparison to Commercial Alloys

The high-temperature steam oxidation of zirconium alloys has been well characterized, with several different known parameters that affect the oxidation kinetics such as alloy composition, gas composition, and oxygen uptake history. The kinetics at 700 °C, 900 °C, and 1100 °C can be easily compared to studies performed by Steinbruck [33, 34], with our lower concentration yttrium alloys experiencing similar kinetics and total weight gains to the better performing M5$^{©}$ zirconium alloy. The lack of sustained linear breakaway oxidation is a deviation from a majority of the alloys oxidized in Steinbruck's work; however, longer exposure periods might be necessary to initiate the oxide cracking responsible for this behavior. The lack of impurities/other alloying elements is one of the driving forces limiting of the transition to breakaway oxidation [15].

Changes in hydrogen uptake have also been observed based on temperature-induced changes in oxidation rate as well as oxide cracking [35]. At high temperatures, hydrogen uptake is increased at localized hot-spots, where the oxidation reaction is increased, as well as where cracking of the oxide allows for a fast path for hydrogen uptake. As the kinetics in this study were found to be diffusion limited in a majority of the cases, the increased hydrogen uptake at higher yttrium concentrations is not attributed to an increase in cracks in the oxide. Linear breakaway oxidation would be observed in the oxidation kinetics if this was the case. Additionally, as the hydride diffraction intensity was normalized to the oxide thickness, increased hydrogen pickup due to a faster oxidation rate will be compensated by the associated increase in oxide thickness. A mechanism that is relevant to the small hydrogen concentration in our 1100 °C samples is the desorption of hydrogen characterized by Große [36, 37]. The continual flow of argon during cooling in our system lowers the partial pressure of hydrogen surrounding the sample, driving additional hydrogen out. The cooling of the system followed an exponential decay, with a decay constant of $1/24\frac{1}{min}$, so the time spent at high temperatures with minimal steam was not excessive.

Conclusions

Thermogravimetric steam oxidation data of Zr-(0.01-1)Y alloys were collected and fit to a power-law oxidation kinetics model. Synchrotron diffraction of samples pre- and post-oxidation was performed to characterize the as-received zirconium lattice and the phases formed during oxidation. Additional optical microscopy was performed to verify hydride intensity results from the diffraction. Below are the conclusions and hypothesis formed from the results.

- The addition of yttrium to zirconium increases the oxidation rate at 500, 700, and 900 °C. Minimal changes are observed at 1100 °C.

- Significant Zr_3O formation occurs at higher temperatures. This is indicative of large amounts of oxygen in solid solution in the Zr matrix.
- Sufficient yttrium and oxide growth are necessary for yttria to form during oxidation.
- Yttrium hydrides can form but are rare compared to zirconium hydrides.
- Zirconium hydride formation increases with yttrium concentration at 500, 700, and 900 °C.
- There appears to be two competing mechanisms effecting the oxidation power-law exponent n: one related to yttrium doping of the oxide which decreases n, and one related to the hydrogen uptake which increases n.

References

1. D. Northwood and U. Kosasih, *International Metals Reviews* **28**, (1), 1983 (92).
2. I. Batra, R. Singh, P. Sengupta, B. Maji, K. Madangopal, K. Manikrishna, R. Tewari and G. Dey, *Journal of Nuclear Materials* **389**, (3), 2009 (500).
3. I. Batra, R. Singh, H. Khandelwal, A. Mukherjee, N. Krishnamurthy, C. Gargi and B. Shah, *Journal of Nuclear Materials* **434**, (1), 2013 (389).
4. C. Li, L. Xiong, E. Wu and S. Liu, *Journal of Nuclear Materials* **457**, 2015 (142).
5. J. Peng, Y. Chen, G. Yan, M. Wu, J. Zhang, L. Wang, J. Li, Z. Guo, in *Advances in Energy and Environment Research: Proceedings of the International Conference on Advances in Energy and Environment Research (ICAEER2016), Guangzhou City, China, August 12–14, 2016* (CRC Press, 2017), p. 43.
6. D. Phalen, D. Vaughan, N. Richard, *Advanced in X-Ray Analysis* **8** (1965).
7. M. Nasrallah and D. Douglass, *Oxidation of Metals* **9**, (4), 1975 (357).
8. L. Fuhrmann, C. Konrad, R. Völkl and U. Glatzel, *Corrosion Science* **94**, 2015 (218).
9. X. Bai, J. Xu, F. He and Y. Fan, *Nuclear Instruments and Methods in Physics Research Section B: Beam Interactions with Materials and Atoms* **160**, (1), 2000 (49).
10. J. Chevalier, L. Gremillard, A. V. Virkar and D. R. Clarke, *Journal of the American Ceramic Society* **92**, (9), 2009 (1901).
11. K. Sridharan, S. Harrington, A. Johnson, J. Licht, M. Anderson and T. Allen, *Materials & design* **28**, (4), 2007 (1177).
12. M. Nasrallah and D. Douglass, *Journal of The Electrochemical Society* **121**, (2), 1974 (255).
13. P.A. Mouche, *Steam Oxidation of Fecral Coated Zircaloy-2*. Ph.D. thesis, University of Illinois Urbana/Champaign (2016).
14. J. Q. Peng, Y. Chen, G. Q. Yan, M. Wu, L. J. Wang and J. S. Li, *Rare Metals* **35**, (4), 2016 (325).
15. B. Cox, in *Advances in Corrosion Science and Technology* (Springer, 1976), pp. 173–3910.
16. H. Porte, J. Schnizlein, R. Vogel and D. Fischer, *Journal of the Electrochemical Society* **107**, (6), 1960 (506).
17. A. Motta, M.G. da Silva, A. Yilmazbayhan, R. Comstock, Z. Cai, B. Lai, in *Zirconium in the Nuclear Industry: 15th International Symposium* (ASTM International, 2009).
18. A. Yilmazbayhan, E. Breval, A. T. Motta and R. J. Comstock, *Journal of Nuclear Materials* **349**, (3), 2006 (265).
19. Y. Sugizaki, S. Yamaguchi, S. Hashimoto, M. Hirabayashi and Y. Ishikawa, *Journal of the Physical Society of Japan* **54**, (7), 1985 (2543).

20. B. Paul Burton, A. van de Walle, H. T. Stokes, *Journal of the Physical Society of Japan* **81**(1), 014004 (2011)
21. B. Holmberg and T. Dagerhamn, *Acta Chemica Scandinavica* **15**, 1961 (919).
22. S. Yamaguchi, *Journal of the Physical Society of Japan* **24**, (4), 1968 (855).
23. J. Bradbrook, G. Lorimer and N. Ridley, *Journal of Nuclear Materials* **42**, (2), 1972 (142).
24. Z. Zhao, M. Blat-Yrieix, J. Morniroli, A. Legris, L. Thuinet, Y. Kihn, A. Ambard, L. Legras, in *Zirconium in the Nuclear Industry: 15th International Symposium* (ASTM International, 2009).
25. S. García-Martín, M. Alario-Franco, D. Fagg, A. Feighery and J. Irvine, *Chemistry of Materials* **12**, (6), 2000 (1729).
26. L. Lanzani and M. Ruch, *Journal of Nuclear Materials* **324**, (2–3), 2004 (165).
27. A. T. Motta and L. Q. Chen, *JOM* **64**, (12), 2012 (1403).
28. R.N. Singh, P. Ståhle, L. Banks-Sills, M. Ristinmaa, S. Banerjee, in *Defect and Diffusion Forum*, Vol. 279 (Trans Tech Publ, 2008), pp. 105–110
29. E. Lacroix, A. Motta and J. Almer, *Journal of Nuclear Materials* **509**, 2018 (162).
30. A. Couet, A. T. Motta, A. Ambard and D. Livigni, *Corrosion Science* **119**, 2017 (1).
31. A. T. Motta, A. Couet and R. J. Comstock, *Annual Review of Materials Research* **45**, 2015 (311).
32. P. A. Mouche, Effects of Hydrogen Uptake and Yttrium Doping on the Oxidation of Zirconium–Yttrium Alloys. Ph.D. thesis, University of Illinois Urbana/Champaign (2018).
33. M. Steinbrück, N. Vér and M. Große, *Oxidation of Metals* **76**, (3–4), 2011 (215).
34. M. Steinbrück, M. Grosse, in *Zirconium in the Nuclear Industry: 17th Volume* (ASTM International, 2015)
35. M. Große, E. Lehmann, M. Steinbrück, G. Kühne and J. Stuckert, *Journal of Nuclear Materials* **385**, (2), 2009 (339).
36. M. Große, M. Steinbrueck, E. Lehmann and P. Vontobel, *Oxidation of Metals* **70**, (3–4), 2008 (149).
37. M. Grosse, M. Steinbrueck, B. Schillinger, A. Kaestner, in *Zirconium in the Nuclear Industry: 18th International Symposium* (ASTM International, 2018).